Volumetric Transformation of Brain Anatomy

Gary E. Christensen,* *Member, IEEE*, Sarang C. Joshi, and Michael I. Miller, *Senior Member, IEEE*

***Abstract*—This paper presents diffeomorphic transformations of three-dimensional (3-D) anatomical image data of the macaque occipital lobe and whole brain cryosection imagery and of deep brain structures in human brains as imaged via magnetic resonance imagery. These transformations are generated in a hierarchical manner, accommodating both global and local anatomical detail. The initial low-dimensional registration is accomplished by constraining the transformation to be in a low-dimensional basis. The basis is defined by the Green's function of the elasticity operator placed at predefined locations in the anatomy and the eigenfunctions of the elasticity operator. The high-dimensional large deformations are vector fields generated via the mismatch between the template and target-image volumes constrained to be the solution of a Navier–Stokes fluid model. As part of this procedure, the Jacobian of the transformation is tracked, insuring the generation of diffeomorphisms. It is shown that transformations constrained by quadratic regularization methods such as the Laplacian, biharmonic, and linear elasticity models, do not ensure that the transformation maintains topology and, therefore, must only be used for coarse global registration.**

***Index Terms*— Brain mapping, global shape models, medical imaging, pattern theory.**

I. INTRODUCTION

MODERN neuroimaging methods allow anatomists to provide exquisitely detailed *in vivo* information regarding the anatomical structure of individual brains. To date, the interpretation of the data has been hindered by the inability to expeditiously relate such information between morphologically varying brains. The difficulty lies in two areas. First images between differing anatomies must be registered. Second, even when registered, normal variation across disparate anatomies makes pooling of interanatomical data difficult, if not impossible.

For the past several years we have been involved in the development of mathematical and computational software tools for the generation of structural representations of brain anatomy which accommodate normal neuroanatomical variation. As we have demonstrated [1]–[7], such representations provide a structural understanding of the brain architecture, invariant to the shape variability inherent to normal brain anatomy. This is in a sense brain representation *modulo normal variation*. To accomplish this, we use the *global shape models* of Grenander [8] to represent the typical global structures in the shape ensemble via the construction of templates, and their variabilities by the definition of probabilistic transformations applied to the templates. The transformations form mathematical groups made up of translations, scales, and rotations and are applied locally throughout the continuum of the template coordinate system so that a rich family of shapes may be generated with the global properties of the templates maintained. Such an approach provides a representation of *normal neuroanatomies*, which precisely specifies the global anatomical relationships between structures as well as how they can vary from one brain to another. The approach taken herein complements the probabilistic atlas approach developed in [9] and [10]. Our methods, however, focus on probabilistic measures associated with the transformations of the coordinate systems of the atlases. This is central to the Grenander paradigm in the pattern theory [8]. From measures of the variation of the coordinate system transformations, estimates on the variations of image intensities at particular locations can be defined.

Preserving geometrical properties and topology during registration is a major thrust of our work. Such properties correspond to topological properties of the transformation such as continuity, differentiability, positive-definiteness of the Jacobian, and others. To this end, we examine diffeomorphic—continuous, one-to-one, onto, and differentiable—transformations in this paper. Transformations that are diffeomorphic maintain topology, guaranteeing that connected subregions remain connected, neighborhood relationships between structures are preserved, and surfaces are mapped to surfaces. Preserving topology is important for synthesizing individualized electronic atlases; the knowledge base of the atlas may be transferred to the target anatomy through the topology preserving transformation providing automatic labeling and segmentation. If total volume of a nucleus, ventricle, or cortical subregion are an important statistic it can be generated automatically. Topology preserving transformations that map the template to the target also can be used to study the physical properties of the target anatomy, such as mean shape and variation. Likewise, preserving topology allows data from multiple individuals to be mapped to a standard atlas coordinate space [11]. Registration to an atlas removes individual anatomical variation and allows information from many experiments to be combined and associated with a single conical anatomy.

The class of diffeomorphic transformations limits registration of brain images to regions of brain anatomy with equivalent topology. These regions typically include deep sub-

---

Manuscript received August 26, 1996; revised December 5, 1996. This work was supported in part by the National Institutes of Health under Grants 7-R01-NS35368-02, R01-MH52158-01A1, and NCRR-RR01380 and by a grant from The Whitaker Foundation. The Associate Editor responsible for coordinating the review of this paper and recommending its publication was N. Ezquerra. *Asterisk indicates corresponding author.*

*G. E. Christensen is with the Department of Electrical and Computer Engineering, The University of Iowa, Iowa City, IA 52242 USA (e-mail: gary-christensen@uiowa.edu).

S. C. Joshi and M. I. Miller are with the Department of Electrical Engineering, Washington University, St. Louis, MO 63130 USA.

Publisher Item Identifier S 0278-0062(97)08962-3.

cortical structures, such as the thalamus, caudate, ventricles, etc. and even some of the major sulci. However, this may be violated such as for various types of disease. Registration of regions with different topology is an area of current research.

There has already been a vast body of work on digital electronic atlases, multimodality image fusion and registration. Digital atlases are currently available [12], especially for colocalization of volume datasets, such as those encountered with positron emission tomography (PET)/single photon emission computed tomography (SPECT), computed tomography (CT) and magnetic resonance imaging (MRI) [13]–[16]. Suitable atlases support neuromorphometric analyzes [17], with both colocalization and neuromorphometric analysis requiring the availability of volumetric image data with large numbers of voxel samples, such as that provided by CT or MRI [9], [18]–[21].

The most straightforward methods of registration assume that the images or tissues being matched are highly similar for which the variability of only global course features are accommodated via affine transformations [11], [21], [22]. We, however, are interested in accounting for very local variability across disparate anatomies, thereby requiring high-dimensional transformations on the coordinate system, the dimension of which are proportional to the number of voxels in the volume. A number of investigators have taken the approach in which the mapping is based on geometric features, such as landmarks (points) [23], [9] and contours (lines) [24]–[30]. Alternatively, others have investigated volume mapping which use the image data directly to generate transformations throughout the coordinate system of the template and target [14], [15], [31]. The voxel image data provide the matching forces throughout the continuum. In our work (see [32]), both approaches are combined via a composition of transformations. The transformations are of high dimension, applied as if the template were a fluid, allowing for the examination of fine features within the continuum of the templates and targets: e.g., cortical folds, sulcal trajectories, deep nuclei, and ventricular volumes and shapes. The transformations on the continuum are tracked and forced to be diffeomorphisms so that all differential geometric features can be mathematically characterized and measured. On the one hand the 20 million parameter transformations are rich enough to map the finest anatomical details; on the other hand, they maintain topology allowing for semantic and geometric features to be mapped. Others have investigated decomposing two-dimensional (2-D) and 3-D nonrigid transformations into separate one-dimensional (1-D) problems [33]. Although 1-D transformations are computationally efficient, 2-D and 3-D transformations constructed from decoupled 1-D transformations still require the reinsertion of the diffeomorphic constraint upon their synthesis to three dimensions.

The paper is organized as follows. Section II describes the coarse-to-fine approach used to transform the shape of an electronic atlas so that it matches the shape of a specific individual's anatomy as imaged via cryosection and MR. Continuum mechanical models based on linear elasticity and fluidity are used to ensure that the high-dimensional transformations preserve topology. These models are concatenated together in the coarse-to-fine procedure for accommodating global and local shape variation between image volumes. Results mapping both 3-D monkey and human anatomical image data are presented in Section III. The validity of the mapping are evaluated by comparing the automatic segmentations generated by mapping the atlas to the target with hand segmentations and directly by composing the forward and inverse transformations.

II. TRANSFORMATION MODELS

A. Mathematical Preliminaries

Populations of anatomies are studied by constructing maps from the population to a common coordinate system. For this, we associate with the single coordinate system an atlas, or template denoted $\boldsymbol{T}$, which is a set of N-registered image volumes $\boldsymbol{T} = \{T_n\}_{n=1}^N$ defined on the coordinate system $\Omega \subset \mathcal{R}^3$ corresponding to different interpretations of a single underlying object of interest. For example, the images T_n can correspond to both sensor readings such as CT and MRI and to logical data such as structure names and functions.

The *target* or *individual* in the population is characterized via a *study* $\boldsymbol{S} = \{S_m\}_{m=1}^M$ defined on Ω consisting of M-characterizing data sets, or substudies. Each substudy is an examination of the target brain tissue via a sensing modality that is in the atlas. In general, the atlas has more modalities than the study, $M < N$ because $\boldsymbol{T}$ usually contains more information than $\boldsymbol{S}$, i.e., segmentation and labeling of structures. The information in the atlas and target coordinate systems are brought into correspondence by finding the transformation $h\colon \Omega \mapsto \Omega$ registering the study $\{S_m\}_{m=1}^M$ with the template $\{T_n\}_{n=1}^N$. Throughout it is assumed that $h(\cdot)$ is constructed from a vector field on Ω according to

$$h\colon x = (x_1, x_2, x_3) \mapsto h(x) = (x_1, x_2, x_3) - (u_1(x), u_2(x), u_3(x)) \quad (1)$$

with the vector field $u(x) = (u_1(x), u_2(x), u_3(x))$ parameterizing the transformation of coordinate systems.

Registration is defined using distance measures $D(h)$ between the transformed atlas and study which are derived from the physics of the sensor. We have used Gaussian distance measures which are appropriate for cryosection and MRI data [34]–[37] and Poisson based distance measures which are appropriate for PET and SPECT data [38]–[41] [emission tomographs, charge-coupled device (CCD) cameras]. For the data presented here the Gaussian distance for one modality was used: $D(h) = \int_\Omega |T(h(x)) - S(x)|^2\, dx$. In a Bayesian framework, the distance measure for N modalities is additive $D(h) = \Sigma_{i=1}^N \; w_i D_i(h)$ assuming independence between modalities conditioned on the coordinate transformation. $D(h)$ is the potential energy of the product of independent probability densities, the distance measures D_i are specific to the imaging modality i, and the weights w_i are associated with each measurement modality.

To ensure diffeomorphic properties, the transformation h is estimated which minimizes the distance measure $D(h)$ while at the same time satisfying *diffeomorphic constraints*. These diffeomorphic constraints are enforced on the transformation h

by constraining the transformation to satisfy the laws of continuum mechanics [42]. The variational problem which is solved is to find the maximum a-posteriori estimators associated with $\hat{h} = \arg\max_h(-D(h) - H(h))$ where $H(h)$ is the energy representation of the regularization on the transformation.

B. Hierarchical 3-D Brain Mapping Protocol

Since 3-D brains are tremendously complex, we have constructed a hierarchical protocol which proceeds from course-to-fine for the generation of the diffeomorphic maps. This protocol has two fundamental pieces, the first poses the registration problem in terms of a series expansion and the second in terms of solving a partial differential equation (PDE) on a spatial grid with dimension on the order of the image lattice (number of voxels). The series expansion involves two series, the first a series which is localized over the input landmarks corresponding to the Green's functions of the elasticity operator and the second a global basis in sines and cosines corresponding to eigenfunctions of the elasticity operator.

The landmark series expansion is based on a natural extension of Bookstein's landmark work [23], [43] in which corresponding points, lines, surfaces, and subvolumes in the template and target are used to drive the deformation. Landmarks can be identified manually or automatically. This step provides an initial global or coarse registration bringing into alignment the major subvolumes and areas of interest. The volume basis series expansion is used to refine the landmark series solution and differs from the landmark expansion in that the volume data itself is used to drive the deformation. The volume basis expansion provides a coarse linear-elastic alignment of the volume for regions in between landmarks. Fine local alignment is accomplished by solving the registration problem posed as the solution of a fluid partial differential equation on a spatial lattice of displacement vectors. The fluid transformation is composed with the small deformation series transformation and may be viewed as using the series expansion solution as its initial condition. We are currently extending the fluid formulation so that it incorporates large deformation theory into the landmark solution [44].

The registrations generated involve several steps organized through three basic transformations which are composed, $h = h_n \circ h_{n-1} \circ \cdots$. The first transformation h_0 applies the affine motions for choosing the best positioning of the template and global scale; subsequent transformations increasing in dimension are the landmark transformations, along with the high-dimensional "small deformation elasticity" and "large deformation fluid transformation." During these transformations the dimension of the vector fields are increased. Initially the affine motions are of dimension 12, increasing to the order of 500 landmarks corresponding to the anterior and posterior commissure lines (Tailarach-like orientation) and the extrenal curves corresponding to the fundi, and finally the PDE-based transformation consisting of 10^6–10^8 dimensions. We are currently extending the landmark based transformation based on small deformation energetics to the fluid formulation to incorporate large deformation diffeomorphic transformation for image registration [44].

1) Landmark Transformation Model: Generating Initial Conditions: The first step in the coarse-to-fine procedure transforms the template into the shape of the target by registering a set of landmarks in the template with a corresponding set of landmarks in the target. The transformation is constrained by a generalized linear differential operator L which can be adjusted to correspond to Laplacian, biharmonic (thin-plate splines), linear elasticity, and other continuum mechanical transformation models.

The affine group $GL(3) \otimes R^3$ (semi-direct product of the translation and generalized linear group) is studied separately from the landmark and image matching transformations. The template is defined to carry the affine motions with it and thus is an orbit, i.e., the equivalence class under the affine group. The affine motion (A, r), which is specified by the 3×3 invertible matrix A and 3×1 translation vector r, is estimated which chooses from the template orbit the instance which is closest to the target. The affine motion accommodates the global scale, rotation, and translation, while the other landmark motions match the globally scaled and oriented template to the target. Throughout, we interpret the maps and elements as vectors in R^3, so that matrix multiplication is understood in the usual sense. The affine motion (A, r) and local vector field transformation $h(x) = x - u(x)$ are estimated jointly from the landmarks.

Define $\{y_i \in \Omega, i = 1, 2, \cdots, N\}$ to be the set of landmarks in the template, identified with varying degrees of accuracy. Associate with each landmark y_i in the template a point x_i identified in the target. Assume that the identification of the points x_i is noisy and is modeled by $x_i - u(x_i) = Ay_i + r + n(y_i), i = 1 \cdots N$, where $n(y_i)$ are Gaussian distributed with a 3×3 covariance Σ_i. The covariance Σ_i represents the spatial variability associated with identifying the landmarks in the data. For the results presented in this paper $\Sigma_i = \sigma_i I$, where I is the 3×3 identity matrix.

The transformation is estimated using the landmark information according to the Bayesian optimization [32], [44]

$$\arg\min_{u,A,r} \int_\Omega ||Lu||^2 + \sum_{i=1}^{N} [Ay_i + r - (x_i - u(x_i))]^t \Sigma_i^{-1} \cdot [Ay_i + r - (x_i - u(x_i))]. \tag{2}$$

For all of the landmark work, we take $L = -a\nabla^2 - b\nabla\nabla \cdot + cI$ with $b = 0$. The solution becomes

$$\hat{u}(x) = \sum_{i=1}^{N} K(x, x_i)\beta_i$$

where $K(x, y)$ is defined by the matrix shown at the bottom of the next page, $\beta_i = [\beta_i^1, \beta_i^2, \beta_i^3]^t \in R^3$ are the weights vectors, and $\alpha = \sqrt{a/c}$. The optimal weights $\hat{\beta} = [\beta_1, \cdots, \beta_N]^t$ and the affine motion $(\hat{A}, \hat{r})$ satisfies the system of linear equations

$$x_i - \left(\sum_{j=1}^{N} K(x_i, x_j)\beta_j - \Sigma_i\beta_i\right) = Ay_i + r \tag{3}$$

$$\sum_i \beta_i y_i = \mathbf{0}, \quad \sum_i \beta_i = \mathbf{0}, \quad i = 1, \cdots, N. \tag{4}$$

The parameters A, r, and β_i are determined by solving the system of linear equations in (3), (4), accomplished by inverting the system matrix.

The procedure to register corresponding curves such as sulci in the template and target is done in a similar manner. Curves are drawn in the data and approximated using a piecewise linear model, assumed to have equal number of equally spaced nodes $\{y_i\colon y_i \in \Omega, i = 1, \cdots, N\}$. The nodes of the template curve are then matched to the corresponding nodes of the target curve.

2) Volume Basis Transformation Model: The second step uses a volume basis transformation model [2], [3], in which the coordinate system of the atlas is transformed as an elastic solid so that it matches the shape of the study. The stress or restoring force grows proportionately to the strain or deformation distance away from the template. One limitation of this model is that it is only valid for small linear deformations. Defining the transformation via the vector field according to $h(x) = x - u(x)$, the strain field $u(x)$ for linear elasticity under the small deformation assumption corresponds to energetics of the form $H(u) = ||L^p u||^2$ where $L = -a\nabla^2 - b\nabla\nabla\cdot + cI$, and $(\nabla\nabla\cdot)u = \nabla(\nabla \cdot u)$. We use the *bending* boundary conditions

$$\begin{aligned}
u_1(x_1, 0, x_3) &= u_1(x_1, 1, x_3) = u_1(x_1, x_2, 0)\\
&= u_1(x_1, x_2, 1) = 0\\
\frac{\partial u_1(0, x_2, x_3)}{\partial x_1} &= \frac{\partial u_1(1, x_2, x_3)}{\partial x_1} = 0\\
u_2(0, x_2, x_3) &= u_2(1, x_2, x_3) = u_2(x_1, x_2, 0)\\
&= u_2(x_1, x_2, 1) = 0\\
\frac{\partial u_2(x_1, 0, x_3)}{\partial x_2} &= \frac{\partial u_2(x_1, 1, x_3)}{\partial x_2} = 0\\
u_3(0, x_2, x_3) &= u_3(1, x_2, x_3) = u_3(x_1, 0, x_3)\\
&= u_3(x_1, 1, x_3) = 0\\
\frac{\partial u_3(x_1, x_2, 0)}{\partial x_3} &= \frac{\partial u_3(x_1, x_2, 0)}{\partial x_3} = 0.
\end{aligned} \tag{5}$$

The eigenvectors for these boundary conditions are

$$\begin{aligned}
\phi_{1,ijk}(x) &= \alpha_{1,ijk}[i \cos ix_1 \sin jx_2 \sin kx_3,\\
&\qquad j \sin ix_1 \cos jx_2 \sin kx_3,\\
&\qquad k \sin ix_1 \sin jx_2 \cos kx_3]^T\\
\phi_{2,ijk}(x) &= \alpha_{2,ijk}[-j \cos ix_1 \sin jx_2 \sin kx_3,\\
&\qquad i \sin ix_1 \cos jx_2 \sin kx_3, 0]^T\\
\phi_{3,ijk}(x) &= \alpha_{3,ijk}[ik \cos ix_1 \sin jx_2 \sin kx_3,\\
&\qquad jk \sin ix_1 \cos jx_2 \sin kx_3,\\
&\qquad -(i^2 + j^2) \sin ix_1 \sin jx_2 \cos kx_3]^T
\end{aligned} \tag{6}$$

with eigenvalues $\kappa_{1,i,j,k} = \pi^2(a + b)(i^2 + j^2 + k^2) + c$ and $\kappa_{2,i,j,k} = \kappa_{3,i,j,k} = \pi^2 a(i^2 + j^2 + k^2) + c$ and normalizing coefficients $\alpha_{1,ijk} = \sqrt{8/(i^2 + j^2 + k^2)}, \alpha_{2,ijk} = \sqrt{8/(i^2 + j^2)}$, and $\alpha_{3,ijk} = \sqrt{8/(i^2 + j^2)(i^2 + j^2 + k^2)}$.

We have also investigated other boundary conditions for the model corresponding to fixed, sliding, bending, and periodic boundary conditions [45].

The variational problem becomes

$$\begin{aligned}
\hat{u} = \arg\min_u \gamma &\int_\Omega |T(x - u(x)) - S(x)|^2 \, dx\\
&+ \int_\Omega ||L^p u||^2 + \sum_{i=1}^{N} [Ay_i + r - (x_i - u(x_i))]^t\\
&\cdot \Sigma_i^{-1}[Ay_i + r - (x_i - u(x_i))]
\end{aligned} \tag{7}$$

where the displacement field u is constrained to be of the form

$$u(x) = \sum_{k=0}^{d} \mu_k \phi_k(x) + \sum_{i=1}^{N} \beta_i K(x, x_i) \tag{8}$$

with the variables $\{\beta_i\}, A$, and r fixed from the landmark transformation. γ is a constant multiplying the distance measure $D(h)$ and is used to adjust relative weight of this term with the energetic constraint terms. The basis functions $\{\phi, \kappa\}$ are the eigenelements of the operator $L, L\phi = \kappa\phi$ corresponding to linear elasticity. Note that various operators can be used for the landmark and the volume basis transformation models. We also note that (8) is valid as a small deformation approximation. Therefore, it is equivalent to composing the first transformation of landmarks h_1 with the additive elasticity basis h_2.

The optimization is accomplished by solving a sequence of optimization problems from coarse to fine scale via estimation of the basis coefficients $\{\mu_k\}$. This is analogous to multigrid methods, but here the notion of refinement from coarse to fine is accomplished by increasing the number of basis components. As the number of basis functions is increased, smaller and smaller variabilities between the template and target are accommodated. The basis coefficients $\{\mu_k\}$ are determined by gradient decent, $\mu_k^{(n+1)} = \mu_k^{(n)} - \Delta(\partial H(u^{(n)}|S)/\partial\mu_k)$, where

$$\begin{aligned}
\frac{\partial H(u^{(n)})}{\partial \mu_k} &= -\gamma \int_\Omega (T(x - u^{(n)}(x)) - S(x))\\
&\qquad \cdot \nabla T(x - u^{(n)}(x)) \cdot \phi_k(x) \, dx + \kappa_k^{2p} \mu_k^{(n)}\\
u^{(n)}(x) &= \sum_{k=0}^{d} \mu_k^{(n)} \phi_k(x) + \sum_{i=1}^{N} \beta_i K(x, x_i)
\end{aligned} \tag{9}$$

with Δ a fixed step size.

$$K(x, y) = \begin{bmatrix} \frac{2(2\pi)^{5/2}}{\alpha} e^{-\alpha||x-y||} & 0 & 0\\ 0 & \frac{2(2\pi)^{5/2}}{\alpha} e^{-\alpha||x-y||} & 0\\ 0 & 0 & \frac{2(2\pi)^{5/2}}{\alpha} e^{-\alpha||x-y||} \end{bmatrix}$$

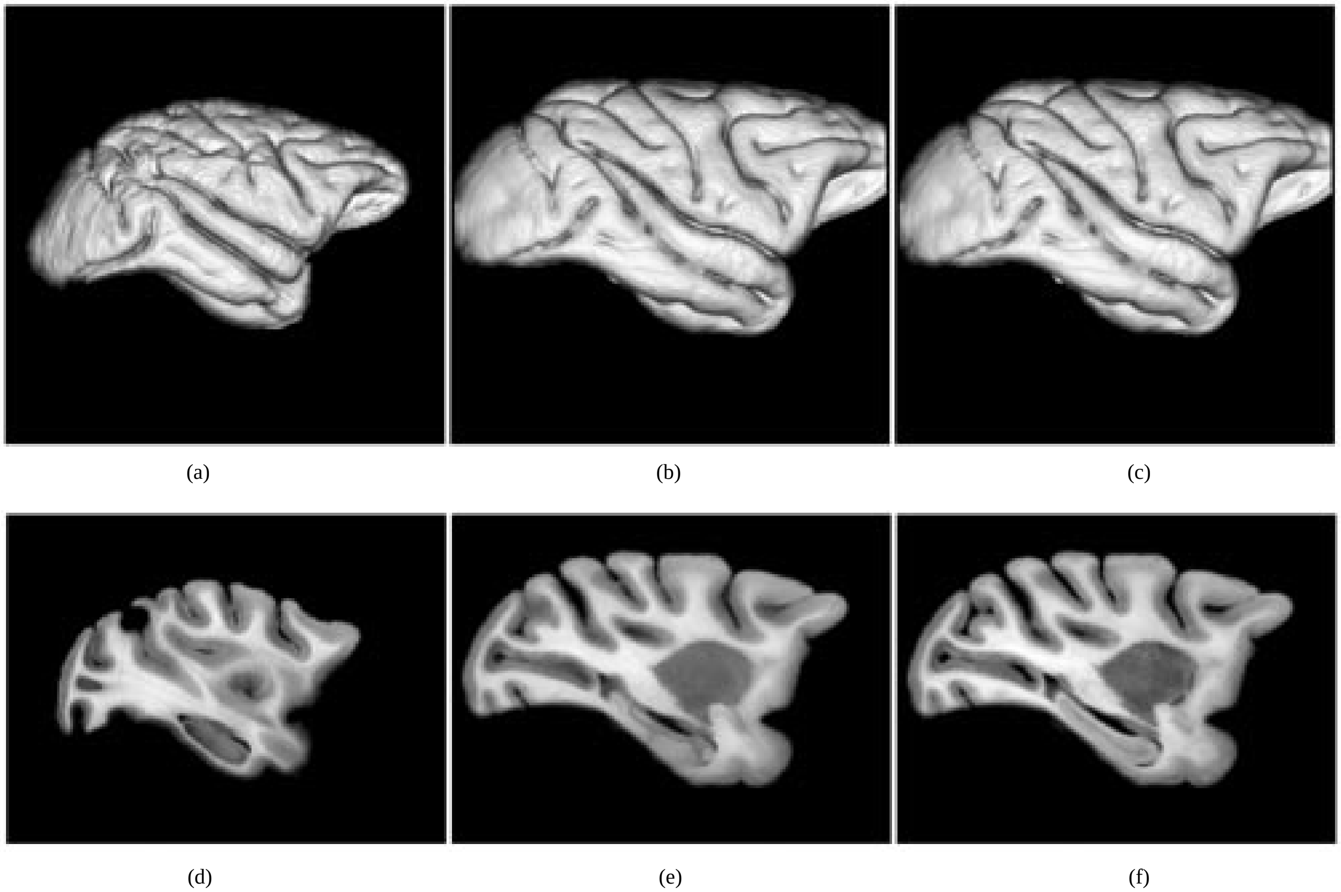

Fig. 1. Three–dimensional transformation of macaque monkey brain hemispheres: 3-D surface rendering of the left hemisphere of the (a) template, (b) the transformed template, and (c) the target image volumes. Cryosection data slice 26 from the (d) template, (e) transformed template, and (f) the target image volumes.

3) The Viscous Fluid Transformation Model: The viscous fluid transformation model [7] accommodates large-distance, nonlinear deformations of the template. For this, an auxiliary random field is introduced, termed the velocity field $v(x,t), x \in \Omega, t \in [0,T]$, which defines the strain vector field $h(x) = x - u(x,T)$ according to

$$v(x,t) = \frac{du(x,t)}{dt} = \frac{\partial u(x,t)}{\partial t} + (\nabla u(x,t))^T v(x,t) \quad (10)$$

for $t \in [0,T]$.

For viscous fluids, the stress grows proportionately to the rate of strain du/dt and forces the mapping to be continuous, 1-1, and onto [7]. Large distance strain distance deformations will occur as long as the rate of strain during the mapping is smooth. The PDE corresponding to the solution of the variational problem for the fluid formulation is given by

$$\alpha \nabla^2 v(x,t) + \beta \nabla(\nabla \cdot v(x,t)) = b(x - u(x,t)) \quad (11)$$

with the boundary conditions $v(x,t) = 0$, $x \in \partial\Omega$, and $t \in [0,T]$. The coefficients α and β are viscosity constants.

The PDE in (11) is nonlinear in $\Omega \times [0,T]$ and is solved via N linear PDE's in Ω for fixed times $t = n\Delta$ where $n = 0, \cdots, N-1$ and $\Delta = T/(N-1)$. The linear PDE's corresponds to (11) with t and $u(x,t)$ fixed and are solved in sequence starting at $t = 0$ and $u(x, t = 0) = 0$. These PDE's are solved numerically for the instantaneous velocity v using successive overrelaxation (SOR) [46] with checkerboard update at each fixed time step. The discrete version of (10) is given by

$$u(x, t+\Delta) = u(x,t) + \Delta(I - \nabla u(x,t))^T v(x,t). \quad (12)$$

Automatic regridding is performed as in [7] and [47], by propagating templates as the nonlinear transformations evaluated on the finite spatial lattice become singular. New templates are propagated when the Jacobian of the transformation of the current template drops below 0.5.

C. Small Versus Large Deformation Models

Due to the complex shape of anatomical structures, it is important that global structures are registered before local structures to avoid local mismatches. With this in mind, the hierarchical mapping protocol progresses from small to large deformation models. The small deformation constraints used in the landmark and volume basis models are only valid for small deformations. Small deformation models do not enforce that the transformation maintains topology for locally large, nonlinear deformations and, hence, are only used to determine nonrigid global correspondence. In order to determine the local correspondence, the large-deformation, viscous fluid model is used which is valid for locally large, nonlinear deformations [7].

The following proposition states formally that small deformation models such as the Laplacian ($b = c = 0$ and $p = 1$), biharmonic ($b = c = 0$ and $p = 2$), and linear elasticity models ($b, c \geq 0$ and $p \geq 1$) do not enforce that transformations maintain topology for locally large, nonlinear deformations. Probabilistic language is used for rigor and because of the duality between minimizing cost functions and maximizing probability.

Proposition 1: Consider transformations of the form $h(x) = x - u(x), u(x) = \Sigma_{i=0}^{d} \mu_i \phi_i(x)$, for $x \in \Omega = [0,1]^m, m \in \{1,2,3\}, d \in \{1, \cdots\}$ where $\phi_1(x), \phi_2(x), \cdots, \phi_d(x)$ are the eigenfunctions of the linear operator $L^p, p \in \{1, \cdots\}$ *and* $L = -a\nabla^2 - b\nabla\nabla \cdot + cI$ with cyclic boundary conditions and a, b, c are positive constants. There exists a set of basis coefficients $\mu_1, \mu_2, \cdots, \mu_d$ with positive Gaussian measure such that the Jacobian of $h(x)$ is negative for a set of x with positive Lebesgue measure.

For brevity, we only prove the 1-D case. The formal proof for higher dimensions is given in technical reports [48], [45]. For $m = 1$, the operator L has the form $L = -(a+b)(\partial^2/\partial x^2) + c$. The operator L^p will have eigenfunctions of the form $\sin \pi i x$ and $\cos \pi i x$. For simplicity, we proceed with only the $\phi_i(x) = \sin \pi i x$ case. The Jacobian of this transformation is given by $J(h(x)) = \partial h/\partial x = 1 - \Sigma_{i=0}^{d} i\pi\mu_i \cos \pi i x$. We now look at $x = 0.5$. Clearly, there is a set $\{\mu_i\}$ with positive Gaussian measure, such that the Jacobian of h at $x = 0.5$ is negative, i.e., there is a set $\{\mu_i\}$ with positive Gaussian measure that satisfies $\Sigma_{i=0}^{d} a_i\mu_i > 1$ where $a_i = i\pi \cos(\pi i/2)$ are constants. The set of x for which $J(h(x)) < 0$ has positive Lebesgue measure because h is a continuous function of x, i.e., there exists an epsilon neighborhood about $x = 0.5$ for which $J(h(x)) < 0$. Q.E.D.

Proposition 1 relates to the regularization functions in (2) and (7) in that the minimizer of $\int_\Omega ||L^p u||^2$ is equivalent to the maximum *a priori* estimate of u given $\mu(u)$.

III. RESULTS

A. Example of Hierarchical Mapping Protocol

To illustrate the overall method of solution, Fig. 1 shows results using cryosectioned data collected from macaque monkey brain hemispheres. The mapping strategy proceeds by initially matching global structures followed by the finest detailed mapping of the local structures. The final transformation was generated by concatenating a sulcal line transformation, with a low-frequency, linear-elastic volume basis transformation, followed by a fluid transformation. Eight sulcal lines were defined in the template and target using VoxelView corresponding to major brain sulci. Each line was parameterized by an ordered set of points. These points (84 total) were matched using (2) to generate the initial global registration. The landmark transformation was refined using an elastic transformation constrained to the first five harmonics. Constraining the elastic transformation to the first five harmonics generated a transformation with

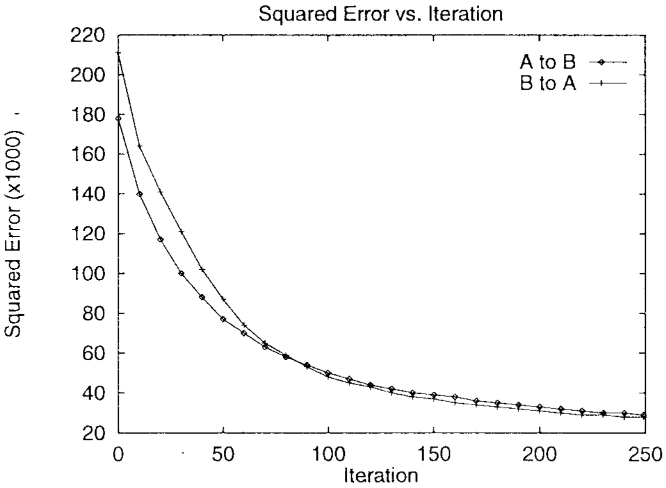

Fig. 2. Plot of the squared error ($\times 10^3$) versus iteration for the transformations of individual A to B and B to A.

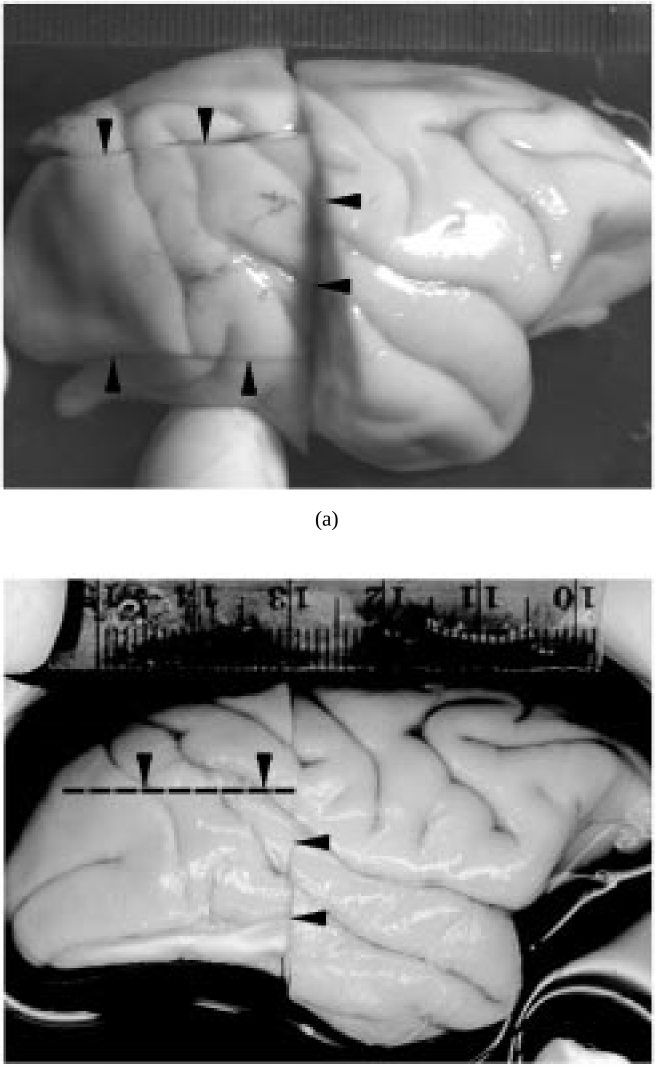

(a)

(b)

Fig. 3. Photograph of the right hemisphere of a macaque monkey used for the (a) template and (b) target. Arrows show the cuts that were made to remove part of the visual cortex.

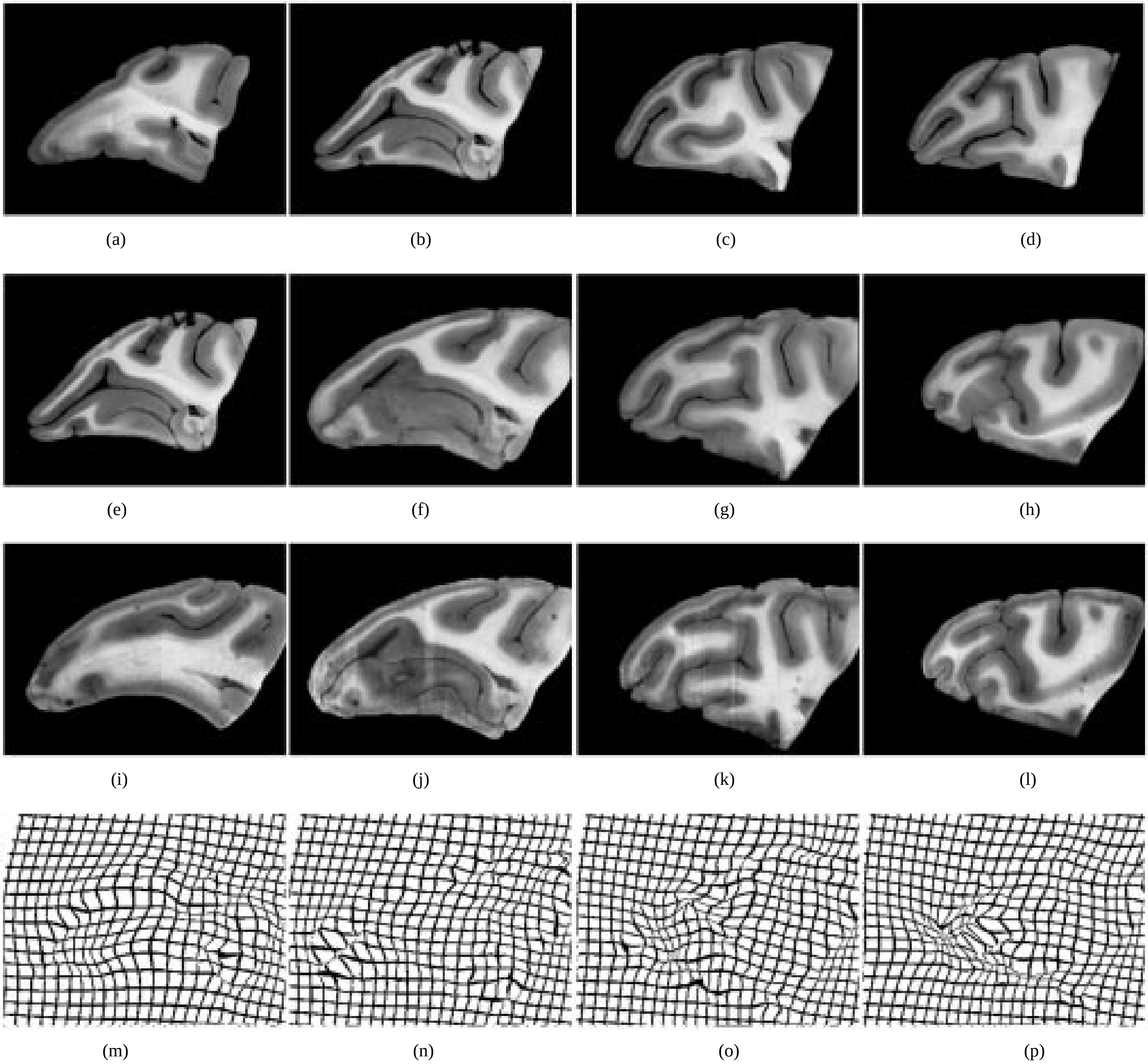

Fig. 4. Parasagittal cryosection occipital cortex slices from the transformation of one 3-D macaque monkey occipital lobe to another: The columns from left-to-right correspond to slices 23, 37, 52, and 61, respectively. (a)–(d) template, (e)–(h) deformed template, (i)–(l) target data set, and (m)–(p) the $x\&y$ projection of the displacement field applied to a 2-D grid.

648 basis coefficients (parameters). This solution was refined by solving the PDE 10, 11 with 500 iterations. The transformed template is depicted in the right column of Fig. 1. This transformation was parameterized by one displacement vector and velocity vector at each voxel location which translates into 5.8×10^6 parameters for the fluid transformation. Notice that this multiresolution procedure generate a transformation image volume that matched both the target macaque brain surface topography and its internal structure. As proven in [7] these maps from the fluid PDE are diffeomorphisms.

The PDE was implemented on the massively parallel DECmpp 12000Sx/Model 200 (MasPar), a 128×128 mesh-connected single-instruction-multiple-data (SIMD) architecture which is well suited for solving partial differential equations such as (11). The 3-D fluid transformation takes roughly 2 h for a $128 \times 128 \times 100$ voxel data set, 100 SOR iterations, and 250 time steps [47].

The solution of the nonlinear fluid PDE (11) is iterative. Fig. 2 shows a plot of the squared difference of the intensities of the deformed template and the target versus number of iterations for the transformation of two $128 \times 128 \times 100$ voxel data sets. The number of iterations used to compute the 3-D fluid transformation was selected to give a good match between the template and target images, i.e. small squared error. Notice that most of the registration occurs in the first 100 iterations of the total 250 iterations generated. This suggests that computation time can be reduced by accepting less precision.

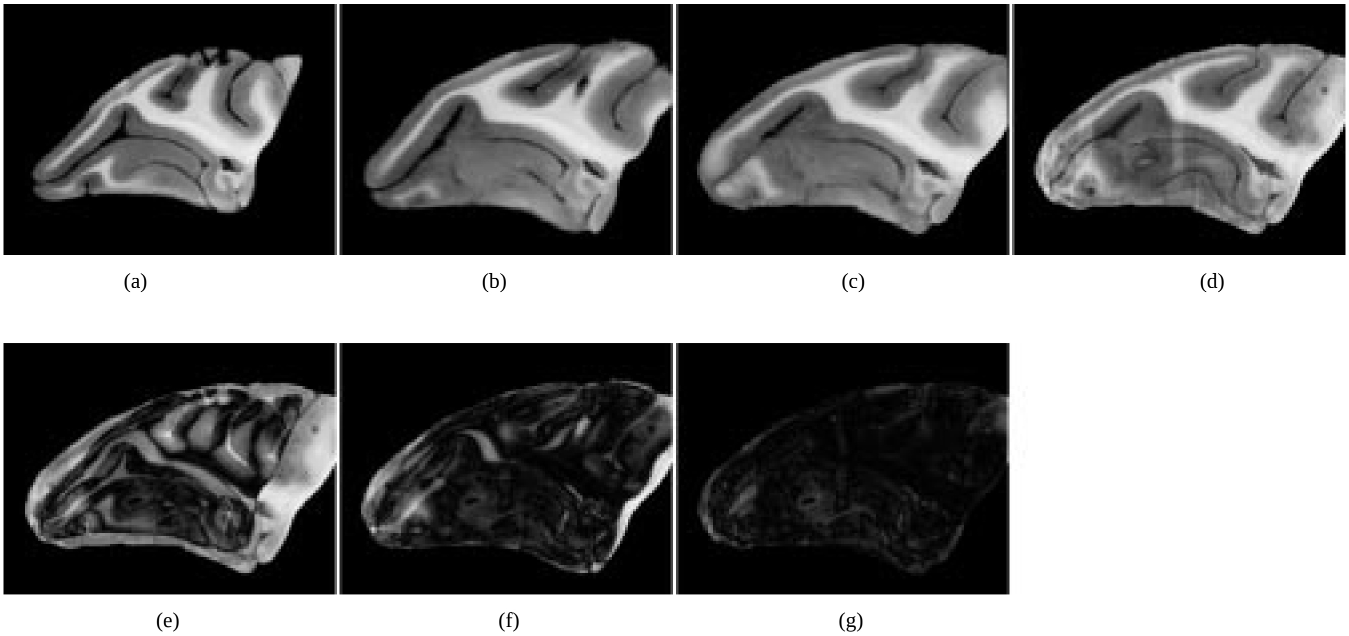

Fig. 5. Intermediate results of the 3-D macaque monkey occipital lobe transformation: Slice 37 from (a) initial template, (b) template after the 312 parameter sulcal transformation, (c) template after the 3.4×10^7 parameter fluid transformation, and (d) the target volume. (e)–(g) Show the magnitude difference images between the target slice and the template after each stage of the transformation.

B. Volume Segmentations and Geometry Generated from Smooth Maps

Generation of the diffeomorphic maps supports the computation of meaningful differential geometric features, such as volumes and surfaces to be preserved and measured. We demonstrate this by taking a more careful look at the neocortex in a subsection consisting of the occipital subvolume of the full macaque brain. Fig. 3 shows a photograph of the macaque cortex used for the atlas [Fig 3(a)] and the target [Fig 3(b)] with arrows denoting the block of brain tissue used. This digital imagery of the occipital lobe was generated in D. Van Essen's laboratory of the Department of Anatomy and Neurobiology at Washington University, St. Louis, MO, by block microtome cryosectioning and CCD digitization of 100-μm sections. The ice surrounding the brain tissue was removed by hand tracing and masking of the brain exterior. The dimension of the template and target data sets were $320 \times 240 \times 64$ and $320 \times 240 \times 54$, respectively. These volumes were symmetrically padded with zeros (the background intensity) to generate equal $320 \times 240 \times 74$ volumes. The target volume was preprocessed by histogram matching its histogram to that of the template volume.

Global registration of the two data sets was accomplished by matching nine major, hand-labeled sulci in the atlas and the target. This transformation was refined to accommodate local variation using the 3-D viscous fluid model to produce the final transformation. The sulcal line information provides initial conditions to the fluid solution; for the fluid model only the volume data provides the driving function. Therefore, hand-labeled sulcal lines could be drawn fairly quickly. The coefficients used for this experiment in (11) were $\alpha = 0.01$ and $\beta = 0.01$.

Fig. 4 shows four slices of the visual occipital lobe of cortex of the template before and after the 3-D hierarchical transformation and the target data set. The bottom row of this figure shows the transformation applied to a rectangular grid.[1] Notice how similar these images appear despite the great initial difference between the template and target. We have chosen these four slices to illustrate major sites of differences in anatomy. Notice how many of them are topologically different when viewed in 2-D, but since the algorithm works completely in 3-D, it moves the folds and surfaces around so as to make them match.

As the template volume deforms in three dimensions into the shape of the target volume, each arbitrary cut through the deforming template begins to look more and more like the corresponding cut in the target volume. Fig. 5 illustrates this improvement as the template deforms into the shape of the target volume after each stage of the transformation procedure for slice 37 in the target anatomy. Slice 37 of the template is initially very different from the target slice 37 as illustrated by the magnitude difference image. The sulcal line transformation accommodates the global nonrigid alignment as shown by slice 37 of the template after the sulcal line transformed and the reduced magnitude difference image. Finally, the fluid transformation accommodates the local shape differences and has the smallest difference image.

The automatic segmentation of the target data set was generated by mapping the atlas segmentation to the target coordinate system. Fig. 6 shows sections from the atlas [Fig. 6(a)–(d)], the automatic segmentation of the target data set [Fig. 6(e)–(h)], and an expert hand segmentation of the

---

[1] The deformed grid images were generated by projecting the transformation for these slices to the x-y plane producing a 2-D transformation. This 2-D transformation was then applied to a 2-D image of a rectangular grid.

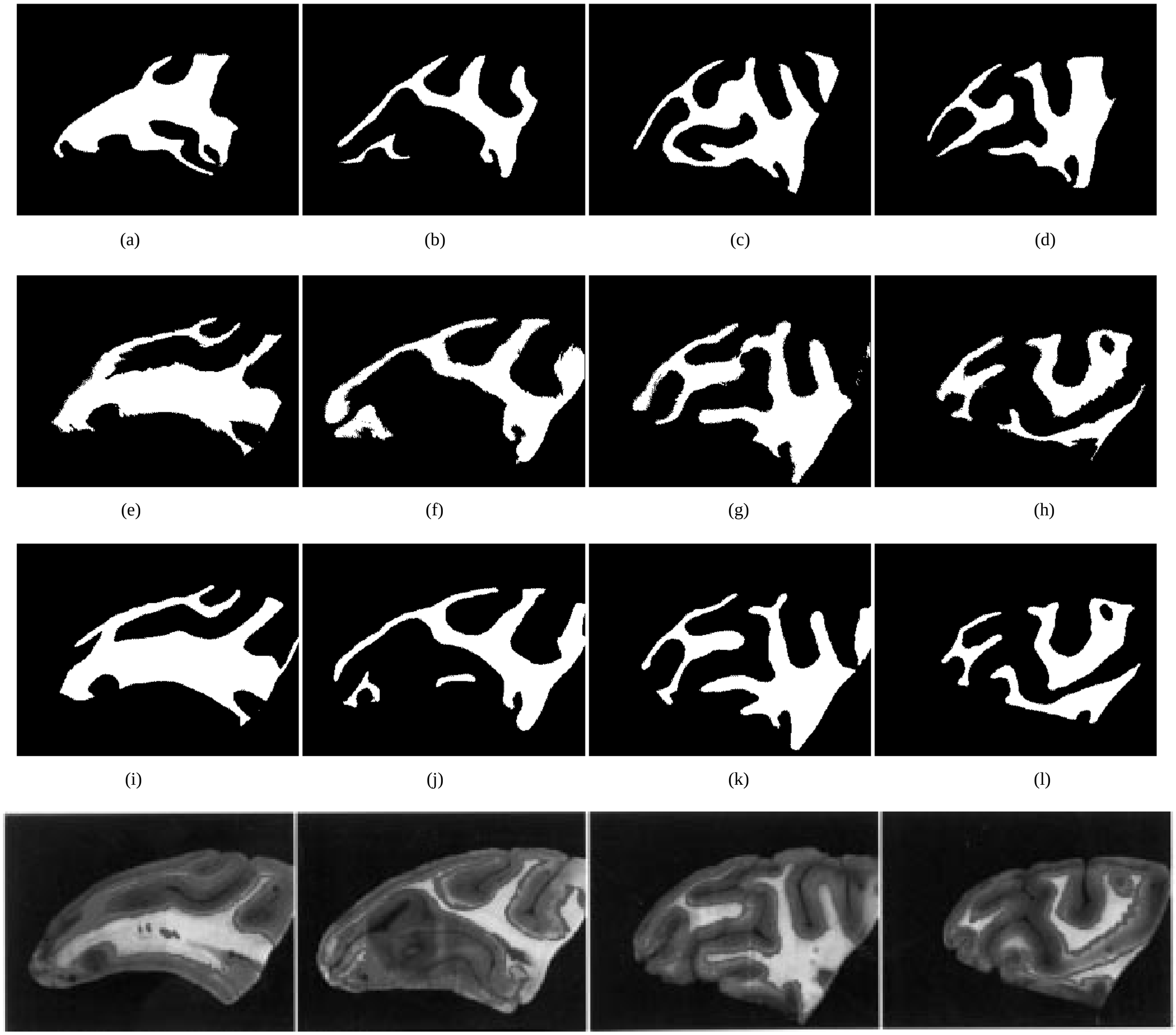
(a) (b) (c) (d)

(e) (f) (g) (h)

(i) (j) (k) (l)

(m) (n) (o) (p)

Fig. 6. Automated 3-D segmentation of occipital cortex volumes. The columns from left-to-right correspond to slices 23, 37, 52, and 61, respectively. (a)–(d) template gray/white matter hand segmentation, (e)–(h) automatic segmentation of the target occipital lobe generated by transforming the template segmentation, and (i)–(l) hand segmentation of the target data set, (m)–(p) gray/white matter surface of the deformed atlas overlaid on the study cryosectioned data.

TABLE I
SEGMENTATION CORRESPONDENCE OF INTERIOR POINTS (SEGMENTATION LABELS ≥ 1 VOXEL FROM A BOUNDARY) FOR THE 3-D MACAQUE OCCIPITAL LOBE STUDY

Structure	Before Transformation percentage	After Sulcal Line Transformation percentage	After Fluid Transformation percentage
background	95.2	97.5	99.9
gray matter	48.6	73.9	94.1
white matter	36.1	66.3	91.8

target data set [Fig. 6(i)–(l)]. Comparison of the Fig. 6(e)–(h) and Fig. 6(i)–(l) shows that the automatic segmentation is close in shape to the hand segmentation. This is further supported by [Fig. 6(m)–(p)] which shows the gray/white matter surface superimposed on the target data set.

It has been shown that segmentation reliability for experts is only valid for points interior to object boundaries [49], [50] (see Fig. 11). To quantify precision of the segmentation protocol, we compute the segmentation correspondence for points interior to object boundaries. Interior points are defined as a template segmentation labels that are one voxel from the object boundary. The segmentation correspondence for interior points is the percentage of correctly transformed interior points to the total number of interior points for each segmented object. This measure takes into account the uncertain nature of segmentation boundaries by using segmentation labels interior to objects.

Table I shows the interior point correspondence for the automatic segmentation of the visual cortex. The left column

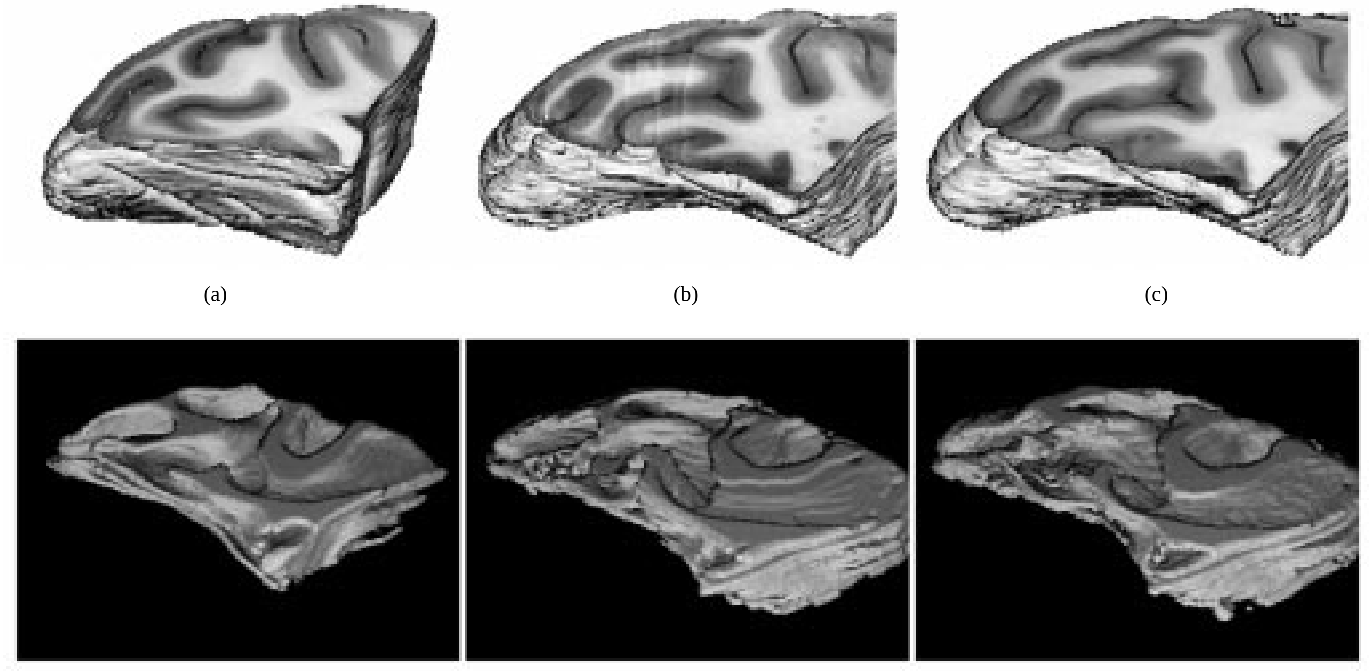
(a) (b) (c)

(d) (e) (f)

Fig. 7. Three-dimensional rendering of macaque monkey occipital lobe transformation: Volume rendering cut at slice 53 of the (a) template, (b) target, and (c) deformed template. Three-dimensional surface renderings of the gray/white matter surface of the (d) template, (e) target, and (f) deformed template.

shows the correspondence before transformation, the middle column shows the correspondence after the 3-D sulcal map solution (the nonrigid global alignment), and the right column shows the correspondence after the fluid solution (the global and local alignment). The top row of the Table I demonstrates the background correspondence of the template and study increased from 95.2–99.9 under the transformation. This implies that the deformed template and study volumes only vary slightly in their over all shapes to give the 99.9 correspondence of the background. Correspondence for the gray matter and white matter regions increased from about 35–50% initially to about 65–75% after the sulcal transformation to nearly 90–95% after the fluid transformation.

Table I also demonstrates the importance of the high-dimensional mapping solution. The middle column shows the alignment for a 200-parameter transformation, which includes the 12-dimensional affine transformation. Even 200 dimensions are not sufficient for providing precise local alignment of the cortical geography. The right column demonstrates the added accuracy of the resulting high-dimensional maps.

We have emphasized that the maps which are generated are diffeomorphic, implying all differential geometric features are maintained. Fig. 7 shows the 3-D volume rendering of the template (left), the target (middle), and the final transformation of the template (right). The bottom row shows views of the gray/white matter neocortical surface being mapped from the template macaque (left column) occipital cortex volume to the target (middle column). The transformation of the template surface is shown in the right column. The right column shows the result of mapping the full occipital cortex volume from the template to the target, and then rendering the surface in the cortical subvolume under the transformation.

C. Results for Human Brain Mapping: Hippocampus Matching

We have developed the algorithm to accommodate not only cryosection data, but also MRI data such as spin density, T1, T2, and MPRAGE sequences. We have mapped several 3-D whole brains as imaged via MRI with the intention of studying the shape and volume of deep structures such as the hippocampus. Shown in Fig. 8 are the results of mapping an entire MPRAGE volume from a single template to two different individual targets. The middle column shows the two different targets (top and bottom rows). The right panel shows the template mapped to the target. This solution involved the computation of $128 \times 128 \times 100 \times 3 \approx 5 \times 10^6$ parameters representing the coordinate system transformation. We have surface rendered the volume data so that the faces are apparent. Notice the phenomenal similarity of the template and target (compare middle and right panels).

We emphasize that the solution does not involve mapping the surfaces alone. Rather, the mapping is based on the entire volume of the heads, which of course carries the surfaces along with internal structures. Our purpose is to study the shape of deep structures such as the hippocampus. To emphasize this, Fig. 9 shows two sections from the 3-D template at its original resolution $1 \times 1 \times 1.25$ mm^3 (left column) and at its interpolated resolution of 0.25^3 mm^3, focusing in on the hippocampus. The segmentation of the template hippocampus was performed by a trained expert at 0.125^3 mm^3 resolution requiring upwards of 20 h to generate.

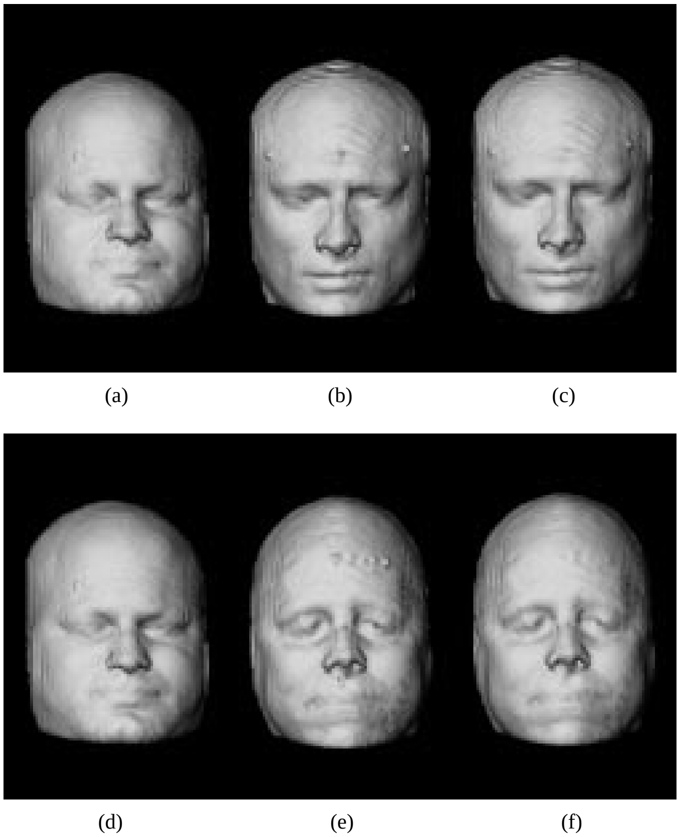

Fig. 8. Three-dimensional MRI-MPRAGE head matching. Surface rendering of the MPRAGE (a) template, (b) target data sets, and (c) 3-D fluid deformation of the template to the target; (d)–(f) same as (a)–(c) for second individual.

This segmentation has a smooth surface so that when the template transformation is applied to the segmentation, it generates a smooth segmentation.

The first step was to perform a landmark transformation on the entire MRI volume ($256 \times 256 \times 128$ voxel volume, with voxel dimension $1 \times 1 \times 1.25$ mm^3). The landmarks were selected to give a coarse alignment of the head while giving a good match in the subregion containing the hippocampus. The landmarks used consisted of the anterior commissure (AC) and posterior commissure (PC), the front and back of the brain on the line defined by the AC-PC line, the top, bottom, left, and right of the brain in the plane perpendicular to the AC-PC line containing PC, the head and tail of the hippocampus, and the top, bottom, left, and right of the hippocampus in the plane perpendicular to the hippocampus head and tail halfway between the head and tail. A $128 \times 128 \times 65$ voxel region at 0.25^3 mm^3 was extracted from the landmark transformed template. The subvolume was generated by transforming the template at 0.25^3 mm^3 resolution and not by trilinearly interpolating the $1 \times 1 \times 1.25$ mm^3 deformed image volume. The template subvolume was fluidly transformed into the target subvolume using 300 iterations of the fluid algorithm. Fig. 10 shows two slices from the original MRI target hippocampus volume (left column), a superimposed segmentation generated by deforming the template to the target (middle-left column), a superimposed hand segmentation (middle-right column), and a difference image of the two segmentations. Notice that all of the error in the segmentation occurs at the edges. Fig. 11 shows that the error in 2-D segmentation of a hippocampus occurs at the boundaries [49].

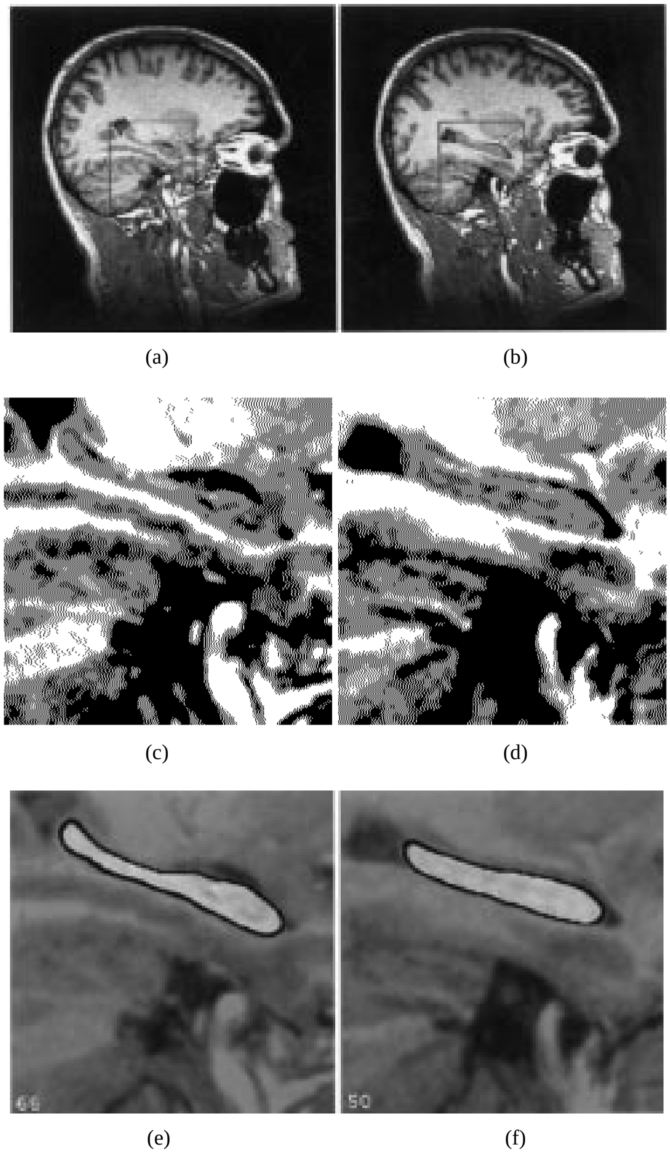

Fig. 9. Sagittal cross section of MRI hippocampus template: (a) and (b) two slices of the MRI template where the hippocampus subvolume is shown in the red box; (c) and (d) the hippocampus subregion from (a) and (b) interpolated to 0.25^3 mm^3 resolution, respectively; (e) and (f) same as (c) and (d) with hippocampus segmentation superimposed, blue corresponds to everything but hippocampus.

Table II shows a comparison between the automatic and manual methods for segmenting the hippocampus in two normal human subjects. The repeated automatic segmentations were generated by placing new landmarks in the target image volume. Percent differences were computed by taking twice the difference between two numbers and dividing by the sum of the two numbers. Notice that there is agreement between repeated manual segmentations and the repeated automatic segmentations. These results are significant considering that the hippocampus is a difficult structure to segment because small errors in segmenting the boundary cause large relative errors in the over all volume [50].

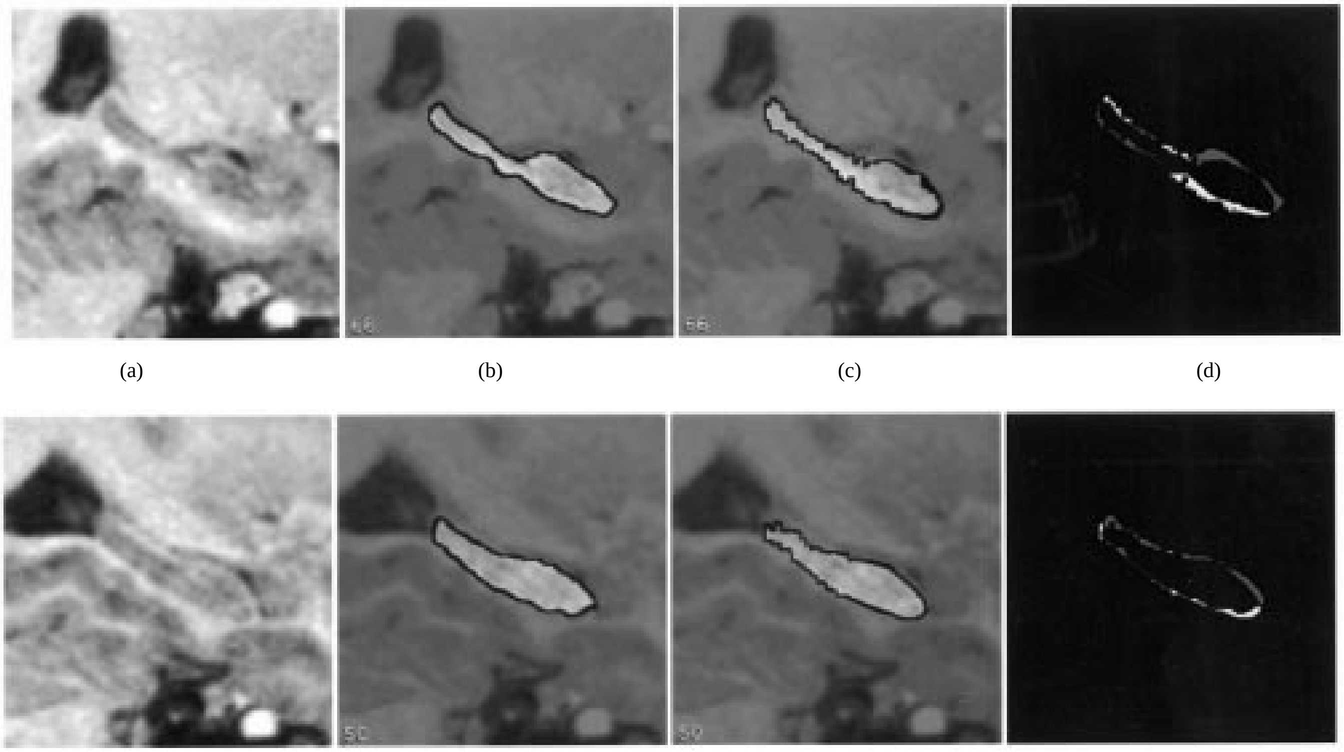

(a) (b) (c) (d)

(e) (f) (g) (h)

Fig. 10. Comparison of automatic and hand segmentation of hippocampus: Two slices from 0.25^3 mm^3 resolution target image subvolume (a) and (e) original, (b) and (f) original with deformed template segmentation superimposed, (c) and (g) original with hand segmentation superimposed, and (d) and (h) difference image between the automatic and hand segmentations.

TABLE II
COMPARISON OF AUTOMATIC AND MANUAL METHODS FOR HIPPOCAMPAL SEGMENTATION

Subject	Auto-1	Auto-2	% Difference	Man-1	Man-2	% Difference	Diff Between Mean of Man and Auto
N1	2842	2849	0.2	2804	3060	8.7	3.0
N2	2825	2922	3.4	2660	2653	0.3	7.8

Precision of the algorithms was evaluated by composing the forward and backward transformations together and measuring the deviation from the identity transformation (see Table III). If the forward and backward transformations are inverses of one another, the composition transformation would be the identity transformation. Two transformations, h_{AB} and h_{BA}, were generated by transforming MRI data set A to B and B to A, respectively. The MRI data used in this experiment were originally $256 \times 256 \times 128$ voxel volumes with voxel dimension $1 \times 1 \times 1.25$ mm^3. These volumes were trilinearly interpolated to have voxel dimension 2 mm^3 and symmetrically zero padded to form a volume of $128 \times 128 \times 100$ voxels. The transformations were generated by concatenating an elastic transformation with the fluid transformation. The elastic transformation was constrained to have harmonics up to $d = 3$ and the fluid transformation was run for 250 iterations. Table III was constructed by projecting each displacement vector from A to B and then from B to A. Each displacement vector from A to B was rounded to the nearest voxel location in B to compute the displacement from B back to A. This procedure causes a small rounding errors. This table shows that the transformations h_{AB} and h_{BA} are almost inverses of each other. Almost 100% of the voxels are mapped to within three voxels of their starting locations, 96% to within two, and 80% to within one.

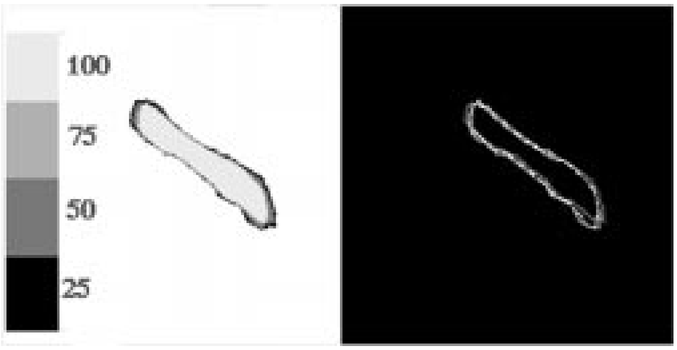

(a) (b)

Fig. 11. (a) The average of four independent segmentations of a 2-D image of a hippocampus and (b) the superposition the contours of all four segmentations. Notice that most of the error in segmentation occurs at the boundaries. Figure reproduced from Haller *et al.*, 1996.

TABLE III
ERROR DISTANCE HISTOGRAM GENERATED BY COMPOSING THE TRANSFORMATION OF A TO B WITH B TO A FOR 128 × 128 × 100 VOXEL TRANSFORMATIONS

Distance	A to B to A		B to A to B	
(voxels)	counts	percentage	counts	percentage
0	610946	37.3	485464	29.6
1	766910	84.1	837036	80.7
2	218616	97.4	249705	96.0
3	31213	99.3	47057	98.8
4	8510	99.9	14776	99.7
5	1822	100	3402	99.9
6	318	100	643	100
7	59	100	235	100
8	6	100	63	100
9	0	100	19	100

IV. CONCLUSIONS

The experiments presented in this paper demonstrate the feasibility of finding diffeomorphic correspondences between anatomies using high-dimensional transformations. Results from mapping monkey and human data show the feasibility in both humans and animals for these techniques. A high-dimensional volume transformation was required to accommodate complex neuroanatomical shape. Global transformations provide a coarse correspondence between two anatomies but fail to provide the local correspondence needed. Specifically, it was demonstrated that the high-dimensional 3-D fluid volume transformation provide a more accurate assessment of the anatomical shape than the 3-D sulcal map transformation or small deformation linear elasticity solution.

Global transformations are computationally inexpensive and the high-dimensional transformations are computationally expensive. Therefore, using the multiresolution approach reduces the over all computational requirements which would be required if of only a high-dimensional transformation is used. The high-resolution, macaque-monkey data demonstrates that the complex cortical mantel can be mapped from one anatomy to another if the resolution of the data permits.

ACKNOWLEDGMENT

The authors would like to thank Dr. D. Van Essen and H. Drury, Department of Anatomy and Neurobiology, Washington University School of Medicine, St. Louis, MO, for providing the histological data. They would also like to thank Dr. J. Csernansky of the Department of Psychiatry, Washington University School of Medicine and Dr. J. Haller and Dr. M. W. Vannier of the Department of Radiology, The University of Iowa, for providing the MRI data, and for their efforts on the mapping tools in the hippocampus studies. They would also like to acknowledge A. Banerjee for his extensive work in the development of the hierarchical algorithm for brain mapping.

REFERENCES

[1] U. Grenander, M. I. Miller, and G. E. Christensen, "Deformable anatomical data bases using global shape models: A position paper for the 1992 electronic imaging of the human body workshop," in *Pro. Cooperative Working Group on Whole Body 3-D Electronic Imaging of the Human Body*, Administered by the Crew System Ergonomics Information Analysis Center, Wright Patterson Air Force Base, Dayton, OH, Mar. 9–11, 1992.

[2] M. I. Miller, G. E. Christensen, Y. Amit, and U. Grenander, "Mathematical textbook of deformable neuroanatomies," in *Proc. Nat. Acad. Sci.*, 1993, vol. 90, no. 24, pp. 11944–48.

[3] G. E. Christensen, R. D. Rabbitt, and M. I. Miller, "Three-dimensional brain mapping using a deformable neuroanatomy," *Phys. in Med., Biol.*, vol. 39, pp. 609–618, 1994.

[4] U. Grenander and M. I. Miller, "Representations of knowledge in complex systems," *J. Roy. Statistical Soc. B*, vol. 56, no. 4, pp. 549–603, 1994.

[5] M. W. Vannier, M. I. Miller, and U. Grenander, "Modeling and data structure for registration to a brain atlas of multimodality images." in *Functional Neuroimaging-Technical Foundations*, R. W. Thatcher, M. Hallett, T. Zeffiro, E. R. John, and M. Huerta, Eds. New York: Academic, 1994, , pp. 217–221.

[6] G. E. Christensen, "Deformable shape models for anatomy," D.Sc. Dissertation, Department of Electrical Engineering, Sever Institute of Technology, Washington University, St. Louis, MO, Aug. 1994.

[7] G. E. Christensen, R. D. Rabbitt, and M. I. Miller, "Deformable templates using large deformation kinematics," *IEEE Trans. Image Processing*, vol. 5, no. 10, pp. 1435–1447, Oct. 1996.

[8] U. Grenander, *General Pattern Theory*. Oxford: Oxford Univ. Press, 1993.

[9] A. C. Evans, W. Dai, D. L. Collins, P. Neelin, and S. Marret, "Warping of a computerized 3-D atlas to match brain image volumes for quantitative neuroanatomical and functional analysis," *Image Processing*, SPIE vol. 1445, pp. 236–246, 1991.

[10] J. C. Mazziotta, A. W. Toga, A. Evans, P. Fox, and J. Lancaster, "A probabilistic atlas of the human brain: Theory and rationale for its development," *Neuroimage*, vol. 2, pp. 89–101, 1995.

[11] J. Talairach and P. Tournoux, *Co-Planar Stereotactic Atlas of the Human Brain*. Stuttgart, Germany: Beorg Thieme Verlag, 1988.

[12] Institute of Medicine, "Mapping the brain and its functions: Integrating enabling technologies in neuroscience research," Tech. Rep. 1991.

[13] T. Greitz, C. Bohm, S. Holte, and L. Eriksson, "A computerized brain atlas: Construction, anatomical content, and some applications," *J. Comput. Assist. Tomogr.*, vol. 15, no. 1, pp. 26–38, Jan./Feb. 1991.

[14] R. Bajcsy, R. Lieberson, and M. Reivich, "A computerized system for the elastic matching of deformed radiographic images to idealized atlas images," *J. Comput. Assist. Tomogr.*, vol. 7, no. 4, pp. 618–625, 1983.

[15] R. Dann, J. Hoford, S. Kovacic, M. Reivich, and R. Bajcsy, "Evaluation of elastic matching systems for anatomic (CT, MR) and functional (PET) cerebral images," *J. Comput. Assist. Tomogr.*, vol. 13, no. 4, pp. 603–611, Jul./Aug. 1989.

[16] K. H. Höhne, M. Bomans, M. Reimer, and R. Schubert, "A 3-D anatomical atlas based on a volume model," *IEEE Comput. Graphics Applicat.*, vol. 12, no. 4, pp. 72–78, 1992.

[17] M. E. Shenton, R. Kikinis, F. A. Jolesz, S. D. Pollak, M. LeMay, C. G. Wible, H. Hokama, J. Martin, D. Metcalf, M. Coleman, and R. W. McCarley, "Abnormalities of the left temporal lobe and thought disorder in schizophrenia," *New Eng. J. Med.*, vol. 327, pp. 604–612, 1992.

[18] W. Jansen, J. P. Baak, A. W. Smeulder, and A. M. van Ginneken, "A computer based handbook and atlas of pathology," *Pathol. Res. Pract.*, vol. 185, no. 5, pp. 652–656, 1989.

[19] C. Bohm, T. Greitz, B. Berggren, and L. Ollson, "Adjustable computerized stereotaxic brain atlas for transmission and emission tomography," *AJNR*, vol. 4, pp. 731–733, 1988.

[20] T. Sandor, F. Jolesz, J. Tieman, R. Kikinis, M. LeMay, and M. Albert, "Extraction of morphometric information from dual echo magnetic resonance brain images," in *Proc. SPIE Visual Communications and Image Processing '90*, 1991, vol. 1360, pp. 665–675.

[21] A. C. Evans, C. Beil, S. Marret, C. J. Thompson, and A. Hakim, "Anatomical-functional correlation using an adjustable MRI-based region of interest atlas with positron emission tomography," *J. Cereb. Blood Flow, Metab.*, vol. 8, pp. 513–530, 1988.

[22] D. L. Collins, P. Neelin, T. M. Peters, and A. C. Evans, "Automatic 3-D intersubject registration on MR volumetric data in standardized Talairach space," *J. Comput. Assist. Tomogr.*, vol. 18, no. 2, pp. 192–205, Mar./Apr. 1994.

[23] F. L. Bookstein and W. D. K. Green, "Edge information at landmarks in medical images." in *Proc. SPIE Visualizat. Biomed. Comput, 1992*, vol. 1808, R A. Robb, Ed., pp. 242–258.

[24] A. W. Toga, P. K. Banerjee, and B. A. Payne, "Brain warping and averaging," *J. Cereb. Blood Flow, Metab.*, vol. 11, no. S560, 1991.

[25] S. R. Sandor and R. M. Leahy, "Toward automated labeling of the cerebral cortex using a deformable atlas." in *Information Processing in Medical Imaging*, vol. 3, Y. Bizais, C. Braillot, and R. Di Paola, Eds. Boston, MA: Kluwer, 1995, pp. 127–138.

[26] C. A. Davatzikos and J. L. Prince, “An active contour model for mapping the cortex,” *IEEE Trans. Med. Imag.*, vol. 14, pp. 65–80, Mar. 1995.

[27] C. A. Davatzikos, J. L. Prince, and R.N. Bryan, “Image registration based on boundary mapping,” *IEEE Trans. Med. Imag.*, vol. 15, no. 1, pp. 112–115, Feb 1996.

[28] D. S. Fritsch, S. M. Pizer, B. S. Morse, D. Eberly, and A. Liu, “The multiscale medial axis and its applications in image registration,” *Pattern Recogn. Lett.*, vol. 15, pp. 445–452, 1994.

[29] A. Hill, T. F. Cootes, C. J. Taylor, and K. Lindley, “Medical image interpretation: a generic approach using deformable templates,” *Med. Informatics*, vol. 19, no. 1, pp. 47–59, 1994.

[30] T. F. Cootes, C. J. Taylor, D. H. Cooper, and J. Graham, “Active shape models—their training and application,” *Comput. Vision, Image Understanding*, vol. 61, no. 1, pp. 38–59, 1995.

[31] J. G. Gee, L. Le Briquer, and C. Barillot, “Probabilistic matching of brain images.” in *Information Processing in Medical Imaging*, vol. 3, Y. Bizais, C. Braillot, and R. Di Paola, Eds., Boston, MA: Kluwer, 1995, pp. 113–125.

[32] S. C. Joshi, M. I. Miller, G. E. Christensen, A. Banerjee, T. A. Coogan, and U. Grenander, “Hierarchical brain mapping via a generalized dirichlet solution for mapping brain manifolds,” in *Proc. SPIE Vision Geometry IV*, vol. 2573, 1995, pp. 278–289.

[33] K. J. Friston, C. D. Frith, P. F. Liddle, and R. S. J. Frackowiak, “Plastic transformation of pet images,” *J. Comput. Assist. Tomogr.*, vol. 15, pp. 634–639, 1991.

[34] E. R. McVeigh, R. M. Henkelman, and M. J. Bronskill, “Noise and filtration in magnetic resonance imaging,” *Med. Phys.*, vol. 12, no. 5, pp. 586–591, 1985.

[35] M. I. Miller and A. Greene, “Maximum-likelihood estimation for nuclear magnetic resonance spectroscopy,” *J. Magn. Reson.*, vol. 83, pp. 525–548, 1989.

[36] T. J. Schaewe and M. I. Miller, “A maximum likelihood reconstruction algorithm for magnetic resonance imaging.” in *Proc. Medical Imaging IV: Image Formation*, R. H. Schneider, Ed., 1990, vol. 1231.

[37] T. J. Schaewe and M. I. Miller, “A model-based approach to magnetic resonance image estimation.” presented at *1993 IEEE Int. Symp. Information Theory*, Hilton Palacio del Rio, Jan. 1993.

[38] D. L. Snyder, Jr., L. J. Thomas, and M. M. Ter-Pogossian, “A mathematical model for positron emission tomography systems having time-of-flight measurements,” *IEEE Trans. Nucl. Sci.*, vol. NS-28, no. 1, pp. 3575–3583, 1981.

[39] M. I. Miller, D. L. Snyder, and T. R. Miller, “Maximum likelihood reconstruction for single photon emission computed tomography,” *IEEE Trans. Nucl. Sci.*, vol. NS-32, no. 1, pp. 769–778, 1985.

[40] M. I. Miller and B. Roysam, “Bayesian image reconstruction for emission tomography: Implementation of the EM algorithm and Good’s roughness prior on massively parallel processors,” in *Proc. Nat. Acad. Sci.*, 1991, vol. 88, pp. 3223–3227.

[41] D. L. Snyder, A. M. Hammoud, and R. L. White, “Image recovery from data acquired with a charge-coupled-device camera,” *J. Opt. Soc. Amer. A*, vol. 10, no. 5, pp. 1014–1023, May 1993.

[42] L. A. Segel, *Mathematics Applied to Continuum Mechanics*. New York: Dover, 1987.

[43] F. L. Bookstein, “The Measurement of Biological Shape and Shape Change,” in *Lecture Notes in Biomathematics*, vol. 24. New York: Springer-Verlag, 1978.

[44] S. C. Joshi, “Large deformation diffumorphisms and Gaussian random fields for statistical characterization of brain sub-manifolds,” D.Sc. Dissertation, Department of Electrical Engineering, Sever Institute of Technology, Washington University, St. Louis, MO, Dec 1997.

[45] G. E. Christensen, S. C. Joshi, and M. I. Miller, “Volume geometric transformations for mapping anatomy,” ECE Department, The University of Iowa, Tech. Rep. 97-7-1, 1997.

[46] J. C. Strikwerda, *Finite Difference Schemes and Partial Differential Equations*. Pacific Grove, CA: Wadsworth & Brooks/Cole Advanced Books & Software, 1989.

[47] G. E. Christensen, M. I. Miller, U. Grenander, and M. W. Vannier, “Individualizing neuroanatomical atlases using a massively parallel computer,” *IEEE Comput., Mag.*, pp. 32–38, Jan. 1996.

[48] G. E. Christensen, S. C. Joshi, and M. I. Miller, “Volume geometric transformations for mapping anatomy.” Monograph ESSRL-96-07, Washington University, St Louis, MO, 1996.

[49] J. W. Haller, G. E. Christensen, S. C. Joshi, J.W. Newcomer, M.I. Miller, J.G. Csernansky, and M.W. Vannier, “Hippocampal MR morphometry by pattern matching,” *Radiol.*, vol. 199, pp. 787–791, 1996.

[50] Y. I. Sheline, K. J. Black, D. Y. Lin, G. E. Christensen, M. H. Gado, B. S. Brunsden, and M. W. Vannier, “Stereological MRI volumetry of the frontal lobe,” *Psych. Res., Neuroimag.*, vol. 67, no. 3, pp. 203–214, Oct 1996.